

# The Use of Annular Dark-Field Scanning Transmission Electron Microscopy for Quantitative Characterisation

**A review of techniques developed for a high resolution study of bimetallic catalysts and other materials**

**By Katherine E. MacArthur\*§**

University of Oxford  
Parks Road, Oxford OX1 3PH, UK

\*Email: [k.macarthur@oxon.org](mailto:k.macarthur@oxon.org)

§Present address: Ernst Ruska Centrum,  
Forschungszentrum Jülich GmbH, 52425 Jülich,  
Germany

Small metallic nanoparticles used for polymer exchange membrane fuel cells (PEMFC) represent a characterisation challenge. Electron microscopy would seem the ideal technique to analyse their structure at high resolution. However, their minute size and sensitivity to irradiation damage makes this difficult. In this review, the latest techniques for overcoming these limitations in order to provide quantitative structural and compositional information are presented, focusing specifically on quantitative annular dark-field (ADF) scanning transmission electron microscopy (STEM) and quantitative energy dispersive X-ray (EDX) analysis. The implications for the study of bimetallic fuel cell catalyst materials are also discussed.

## 1. Introduction

It is well established that catalyst nanoparticles are critical to the success of PEMFC; indeed it is

the cost of the platinum loading which currently limits their wide-scale use. To help the search for better catalysts, with higher catalytic activity and specificity and lower cost, steady improvement in characterisation abilities is essential. Since the technique's infancy (1), ADF STEM has been utilised for the study of catalysts due to the strong dependence of signal intensity on atomic number (see **Figure 1**). This so-called 'Z-contrast' has enabled differentiation of individual heavy atoms from lighter, and even crystalline, supports well before atomic resolution was even possible, as first demonstrated by Crewe, Wall and Langmore (1) and later by Nellist and Pennycook (2) among others. STEM suffers from the inherent problem of many other high resolution techniques, where the particularly small area investigated may not be representational of the whole sample. However the technique does provide the local atomic scale information which is essential to completely understand catalysts at the same length scales as their chemical reactions.

This paper will introduce the key advantages and limitations of STEM for materials characterisation. Some of the more recent advances and developments in the field of quantification, where the machines are beginning to be used much more as analytical tools rather than high resolution cameras, will also be discussed.

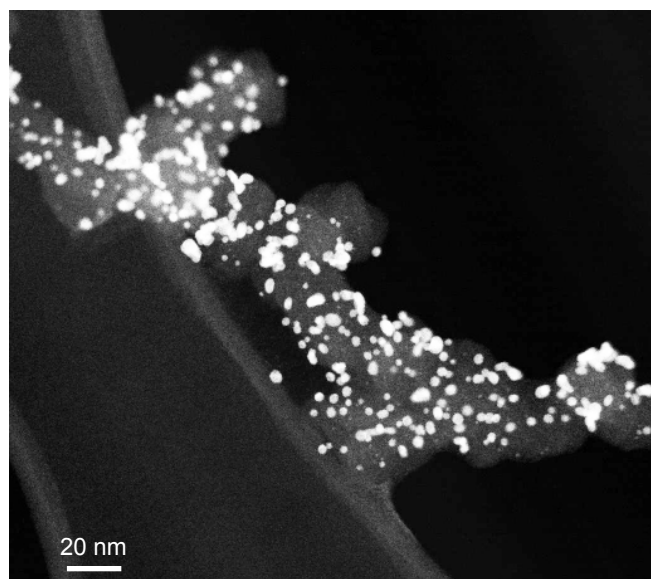


Fig. 1. Example of a low magnification ADF STEM image of Pt(Pd) core-shell catalyst nanoparticles which show up much more brightly than the low atomic number carbon black support. Image was taken on a Jeol atomic resolution microscope (ARM)

## 2. The Fundamentals of Scanning Transmission Electron Microscopy

STEM is a process where pre-specimen lenses focus the beam into a small probe that is scanned in a raster pattern across the sample (see [Figure 2 \(a\)](#)). This

is similar to scanning electron microscopy (SEM) (3) except that here the transmission signal is collected and it is customary to use an electron transparent transmission electron microscopy (TEM) thin foil, producing significantly improved resolution because beam-spreading or particle scattering events are reduced in thin samples. There are a variety of signals emitted by the sample due to excitation from the high energy electron probe (see [Figure 2 \(b\)](#)). One of the major advantages of STEM is the ability to detect several of these signals in parallel. The collection of several signals in parallel is particularly beneficial for beam sensitive samples, such as catalysts, as they will often damage or reconstruct during analysis due to the high energy provided by the electron beam. This means that sequential images will not present the same sample structure, especially at atomic resolution.

A small on-axis detector, with an outer collection angle typically less than 5 mrad, produces a bright-field (BF) STEM image. The origin of the image contrast is the interference between overlapping Bragg disks (these disks are green in [Figure 2 \(a\)](#)). Due to the theory of reciprocity (5) BF-STEM, with a convergent illumination and a small on-axis detector, is analogous to BF high resolution TEM, with a small point source and a large detector collecting the resultant scattered beams. A disadvantage of both methods is that they suffer contrast inversions with defocus and thickness,

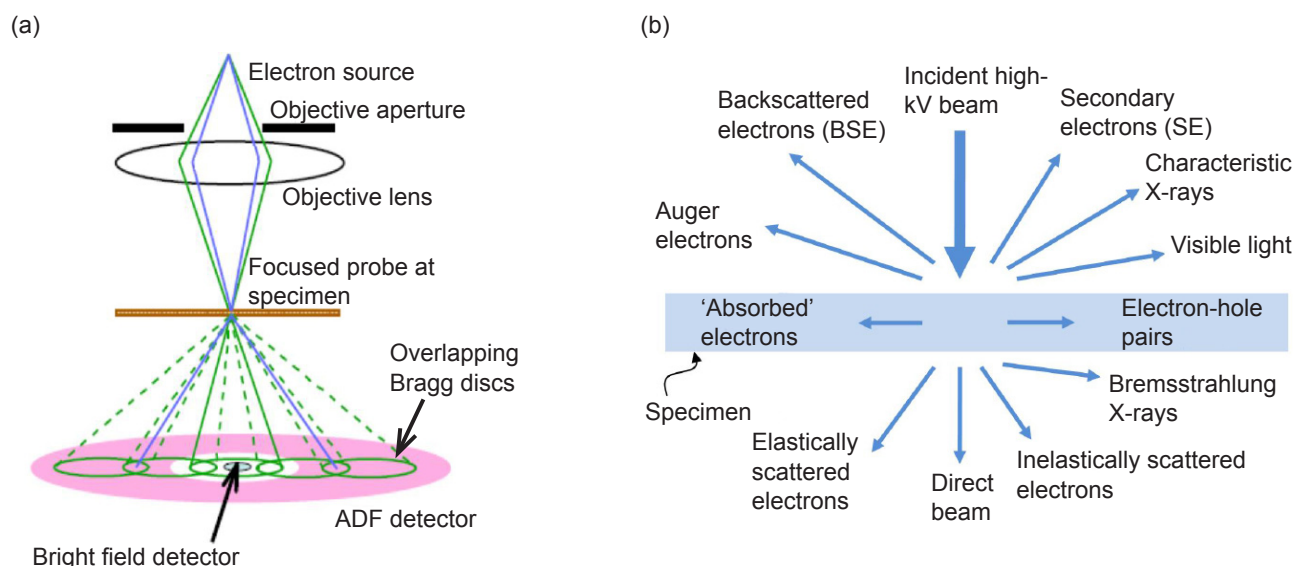


Fig. 2. (a) Schematic of image formation in a STEM, showing the on-axis small bright-field detector and the larger annular dark-field detector, pink; (b) signals generated when a high-energy beam of electrons interacts with a thin specimen. The directions shown for each signal do not always represent the physical direction of the signal but indicate, in a relative manner, where the signal is the strongest or where it is detected. Image (b) was redrawn from Williams and Carter (4)

and difficulties associated with image interpretation of a coherent signal (4). A recent approach aims to produce a more incoherent BF image by using an annular detector, referred to as annular bright-field (ABF). The theory is that ABF is more sensitive to lighter elements like oxygen or lithium (6–8), although the exact origin of the image contrast is still a matter of debate so whether or not quantitative intensity information can be extracted is uncertain.

Using an annular detector to only collect the electrons scattered to higher angles, typically larger than 80 mrad, often referred to as high angle annular dark-field (HAADF), produces a coherency loss in the signal detected. Originally, Howie proposed (9) that the cause of this coherency loss was thermal diffuse scattering (TDS) at larger detector angles becoming the more dominant scattering mechanism over elastic or Bragg scattering. However, it was later demonstrated that the process of integration of the signal over a large annular detector, and therefore a large range of scattering angles, is the cause of the coherency loss. Any dynamical elastic diffraction of electrons scattered onto the detector will have no effect on the final image as the intensity is only redistributed elsewhere in the detector and is still integrated into the total collected signal (10). ADF STEM produces an image with atomic number sensitivity or Z-contrast following power law relationship  $Z^\alpha$ , where  $\alpha$  is between 1 and 2 depending on the angular range of electrons collected (11) and relative Debye-Waller factor between atoms among other things. Many early attempts at intensity quantification have relied on accurately characterising this exponent.

## 2.1 Aberration Correction

Unlike optical lenses, electromagnetic lenses contain inherent aberrations that are unavoidable (4, 12, 13). When aberration correction is discussed it normally refers to correction of the positive spherical aberration,  $C_s$  or  $C_3$ , in which the rays furthest from the optic axis are focused more by the lens field. In early instrumentation, namely TEM, resolution was improved by using higher accelerating voltages (14) in order to minimise the sample interaction volume, a process which inevitably had its own limitations due to the resulting high damage rates. Later it was combatted by using a so-called high-resolution or narrow gap pole piece with a much smaller  $C_s$  of 0.7 mm (15). However, the narrow gap produces large restrictions on specimen holders, including tilt ranges and *in situ* cells and limits

the possible additional detectors for microanalysis. The most recent solution is an aberration corrector, where a series of non-round lenses are used to counteract the aberrations, similar to the lenses in glasses for eyesight improvement. In STEM this results in not only a reduced probe size (improving resolution) but also an increase in the current density within this corrected probe (16), causing an enhanced signal-to-noise ratio (SNR) during imaging and significant improvement in counts for microanalysis. Aberration correctors allow microscopes to keep their large pole piece gaps and are now commercially available, existing in microscopes around the world (16–19).

## 3. Quantification of Annular Dark-Field Images

ADF STEM images are easy to interpret qualitatively due to the Z-contrast nature of the technique and the absence of any contrast inversions with thickness. The information they can provide when images are treated as data sets and analysed quantitatively is only just beginning to be explored. Often what people mean by ‘quantification’ is a comparison with simulated images. Anderson *et al.* (20) scaled simulated images to fit with experimental data rather than acquire them on an absolute scale. Darji and Howie (21) have also discussed the necessity of correcting experimental data; in this case for additional scattering from a crystalline substrate, as they believed this was the origin of the mismatch between experiment and simulation. Meanwhile for TEM there is a widely accepted mismatch between simulation and experimental intensity known as the Stobbs factor (22).

The earliest attempts on quantification were by Retsky (23) and Isaacson *et al.* (24) in the 1970s, comparing the integrated intensity of heavy metal atoms or small clusters to those values calculated from first principle quantum mechanics. Work on small metallic clusters has often assumed that the integrated ADF intensity of a cluster scales linearly with the number of atoms it contains (25, 26). Therefore if the intensity of a single atom is known, dividing the total intensity of a cluster by this value yields the cluster size in atoms. It is an acceptable approximation for amorphous and off-axis clusters where it can be assumed that no channelling (see below) is occurring. However, it is overly simplistic to assume such linearity for on-axis crystalline particles and neglecting coherency effects in calculations is likely to cause significant errors.

### 3.1 Channelling

For direct interpretation of images and accurate quantification, on a column by column basis, cleanly resolved atomic resolution images are required. This necessitates viewing the sample down a low order zone-axis (27). When atoms are aligned in this way, parallel to the incident electron probe, they provide a small lensing and therefore focusing effect on the beam (28) (see **Figure 3**). The subsequent atoms in the atomic column then experience a more focused probe than the first atom; resulting in the amount of scattering to the detector initially increasing faster than linearly with respect to the number of atoms. Therefore the contribution of the second atom in a column to the integrated intensity (the summed value of all the pixels within the image which represent one feature) or the total scattering cross section (29) of the column is larger than the contribution of the first and so on. Along a longer column, oscillations in intensity are seen (30) and the process is often referred to as channelling. TDS simultaneously leads to a reduction in the electron intensity along a column which is often referred to as absorption. Channelling has considerable implications for ADF STEM if not taken correctly into account (27, 29, 31, 32). Heavier atoms provide a stronger lensing effect than lighter atoms, which means that in columns containing a mixture of atom types the specific sequence of the atoms in the column will affect the resulting intensity scattered out to the detector (33).

In certain circumstances channelling can be exploited to expose subtle sample changes; for example it has been used advantageously to map the height of

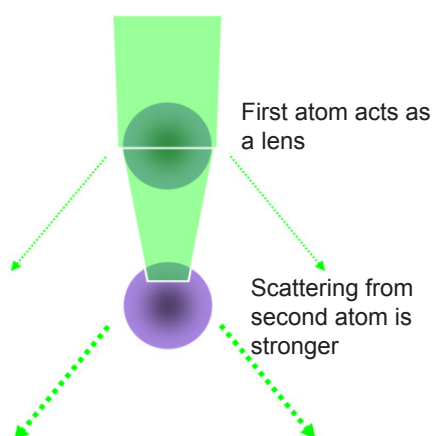


Fig. 3. Schematic of how a column of atoms focuses the STEM probe producing a stronger scattering and therefore a higher intensity than the atoms would produce individually

dopant atoms within an atomic column based on their contribution to the image intensity (34–37).

### 3.2 Detector Calibrations

The more common method of ADF STEM quantification utilises a detector normalisation method pioneered by Singhal, Yang and Gibson (26), and LeBeau and Stemmer (38), as such it is essential to be able to understand and map the efficiency of the STEM detectors. Commercially available ADF detectors consist of a scintillator, a glass light pipe and a photomultiplier tube (PMT). The scintillator is normally either a powder  $\text{Y}_2\text{SiO}_5$  doped with cerium, a single crystal made of yttrium aluminium garnet (YAG) or, more commonly, yttrium aluminium perovskite (YAP). Electrons hitting the scintillator are converted into a photon cascade. The photons are directed to a PMT through the light pipe and converted into an electrical signal, which can be controlled to vary the 'contrast' in the final image. A constant voltage (direct current offset) may be added by a preamplifier, controlling the 'brightness' in the final image. Finally the output is digitised by an analogue to digital converter and sent to the computer. When aiming for a truly quantitative comparison with simulations it is important to map and understand the detector efficiency, as most simulation software packages normally assume a perfect detector, modelled by a uniform efficiency mask.

The more common method of detector mapping relies on using a confocal arrangement, referred to as STEM 'alignment' mode. The post specimen lenses are adjusted to translate an image of the probe at the specimen plane onto the detector plane (see **Figure 4 (b)**). This produces a fine convergent beam which can be scanned over the detector; recording the detector output with respect to probe position provides a map of the detector efficiency. The gain and DC offset are optimised from the detector map such that the maximum range of signal is achieved without saturating the detector or clipping any of the pixels in the vacuum (38).

The alternative 'pencil beam' method of detector scanning (26) may provide a more realistic map in angle space (because of how the beam passes through the post specimen optics); the beam is travelling tilted from the optic axis. This was the more traditional method of detector mapping used in dedicated STEMs where no post specimen lenses were present due to the way in which the beam passes through the post-specimen optics. The convergence angle of a



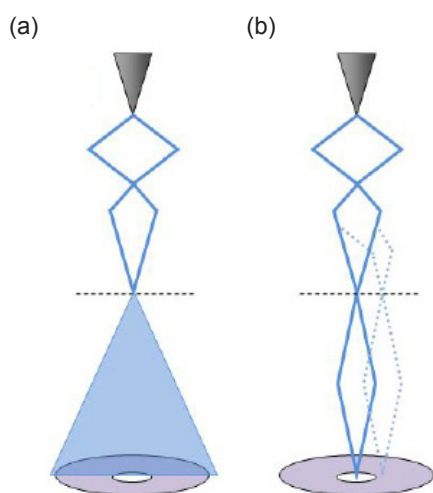


Fig. 4. (a) Ray diagram of a STEM with the electron flux seen by the detector due to scattering from the sample; (b) scanning confocal geometry where the image of the probe at the specimen plane is transferred to the detector plane

typical STEM probe is around 20 mrad, whereas the angle of scattering out to the detector can be up to ten times that. These scattered electrons will interact with post specimen lenses at a very large tilted angle where lens aberrations are normally worse, making it beneficial to map the detector in angle space. However, it is more difficult to set up and thus its use so far has been limited to dedicated STEM machines.

When using detector normalisation for quantitative analysis it is important to be aware of the linearity of the detector response (38–40). In particular, altering the detector contrast does not produce a linear variation (41) in the detector signal, which is why contrast and brightness settings are normally kept constant between detector mapping and experimental images.

The majority of image intensity detector normalisation methods rely on the detector responding linearly with the number of incident electrons. Care should be taken not to rely too heavily on this linearity alone. During experimental image acquisition the detector will see a diffuse electron flux (see Figure 4 (a)) at a much lower intensity, whereas during detector mapping the whole beam is scanned over it in a fine probe. To combat this it is prudent to drop the probe current by a known amount during the detector mapping (42) and subsequently incorporate a ratio of the probe currents into the quantification method. Lowering the current also helps to minimise damage to the detector and makes a greater contrast range available in the final experimental image, which is particularly useful

for imaging nanoparticles or other low dimensional materials.

Working from the premise that real detectors are asymmetric in their collection efficiency (43, 44) there needs to be a way to compensate for this to improve matching with simulations. Rosenauer *et al.* (39) use a two-dimensional (2D) profile estimate of their detector asymmetry to simulate images with an asymmetric detector; however this approach is only possible with certain simulation packages. The flux weighting method developed by Martinez *et al.* (45) aims to improve the detector normalisation by accommodating for this asymmetry in the experimental images rather than adjusting the simulations.

### 3.3 Recent Advances in STEM Quantification

LeBeau and Stemmer are generally acknowledged as the originators of a resurgence of interest in detector calibrations and recording images on an absolute intensity scale (see Figure 5) (38). Their method relies on a full characterisation of microscope imaging parameters and detector responses in order to achieve direct comparison with simulations (46), although defocus has been fitted empirically from selecting the simulated image which fits most closely to experimental images.

Quantitative comparison between experiment and simulation has only become possible due to improvements in parallelisation of simulation software, first on central processing units (CPU) and then graphical processing units (GPU). Such parallelisation makes it possible to produce accurate simulation reference libraries in reasonable time-scales using the more accurate (but more computer intensive) frozen phonon approach rather than absorptive potential (47).

From a detector efficiency map like the one presented in Figure 6 (b), the average pixel intensity in the active region (the area coated with the scintillator, predominantly blue in Figure 5 (b)) can be considered to represent one hundred percent of the total electron beam, whilst the average intensity of the background region (anywhere in the image detector image considered not to be the active region) represents no-beam and is also known as the black-level. Normalising experimental images using these maps results in images being scaled as a fraction of the incident beam which has been scattered out to the detector.

An improvement to this has been developed by calculating the scattering cross-section (29) or

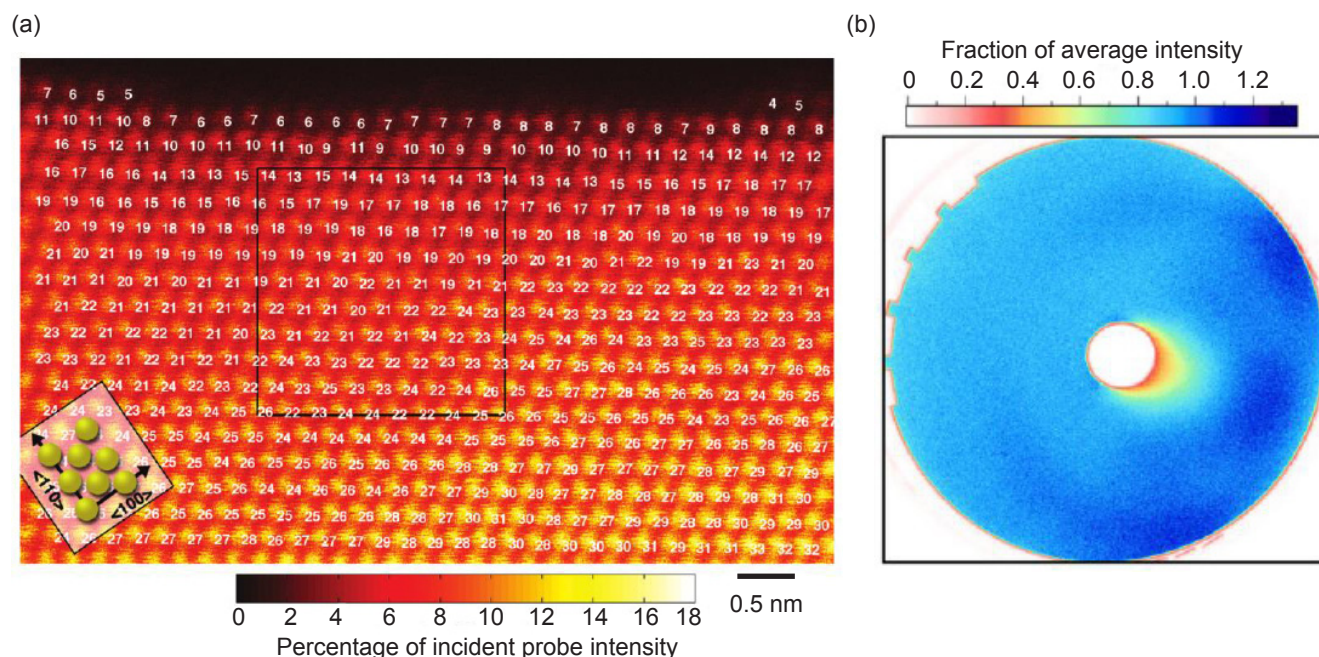


Fig. 5. (a) One of the first ADF STEM images normalised to the incident beam. The sample is a gold wedge and the white numbers represent the assigned atom counts based on direct comparison with simulation; (b) the associated detector efficiency map in units of fraction of the average intensity of the active region. (Reprinted with permission from (46). Copyright (2010) American Chemical Society)

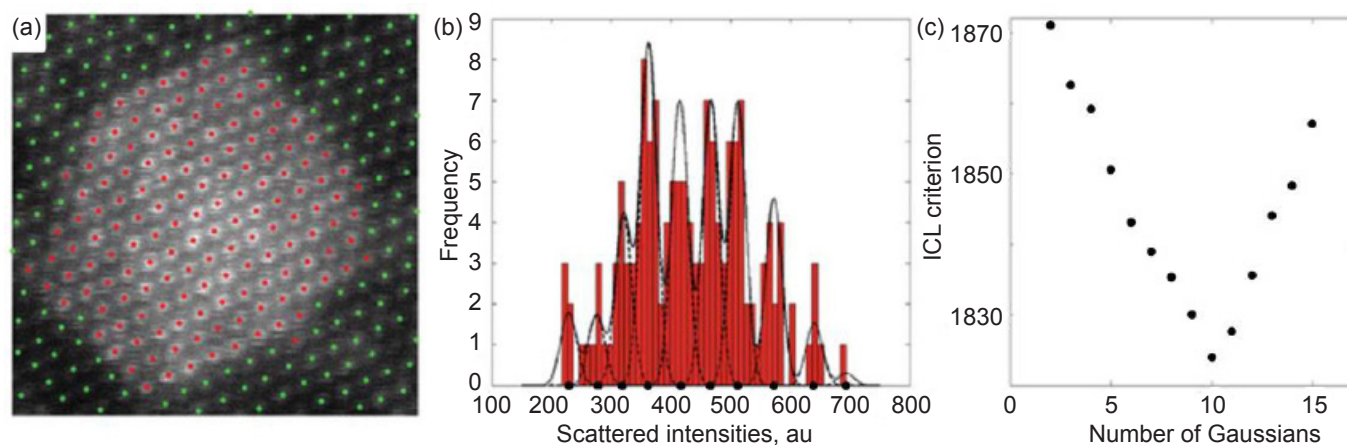


Fig. 6. (a) Image of a silver nanoparticle embedded in an aluminium matrix, the dots represent the estimated position of the atomic columns with those assigned as silver marked in red; (b) histogram of the scattered intensities of the Ag columns. The black solid curve shows the estimated mixture model; the individual components are shown as dashed curves; (c) the ICL criterion evaluated as a function of the number of Gaussians in a mixture model. The minimum at 10 components represents the optimum number of components (Reprinted by permission from Macmillan Publishers Ltd: Nature (59), copyright (2011))

Gaussian volume (31, 48) of each atomic column within an image. Scattering cross-sections are calculated by integrating the normalised intensity over one atomic column, using a Voronoi polygon (49, 50) or otherwise, and multiplying by pixel area. This creates a value with area units that represents the probability

of electrons interacting with that column and scattering out to the ADF detector, much in the way that other cross-sections behave in particle physics. Gaussian volumes are mathematically identical to cross-sections (51), only instead of integrating the intensity in a polygon method, a 2D Gaussian curve is fitted to the

image intensity of each column and the integrated volume under this curve is used. Using these volumes or cross-sections for quantification still requires comparison with simulations but is a lot more robust to defocus, tilt, source size and other aberrations (29, 32, 48). Although the robustness of such an integration or averaging over a unit cell has been commented on before (20, 39, 52), it was not until the scattering cross-section work (29, 32, 48, 51) that it was mathematically proven and robustly tested through a series of simulations. Scanning distortions may still affect the quantification accuracy; recent advances in non-rigid image registration may provide the solution to this (53–55).

An alternative technique to direct comparison with simulation is one based on statistical parameter estimation theory (56), pioneered by Van Aert *et al.* (57). The theory relies on the inherently quantised nature of a histogram of integrated intensities from an experimental image (58). For a single element scenario, for example the silver particle in **Figure 6**, the integrated intensities should naturally be quantised in the histogram due to the fact that each column contains an integer number of atoms. These discrete values become somewhat smeared by Poisson noise and other random errors; however, it should still be possible to decompose the histogram of all the integrated intensities into a series of Gaussian components through statistical estimation and a maximum likelihood criterion. The critical component of this algorithm is a ‘cost function’ to minimise the total number of Gaussians incorporated, otherwise the best solution would be an infinite number of Gaussians. The integrated classification likelihood (ICL) criterion is used for this purpose and provides a local minimum at the optimum number of components (**Figure 4 (c)**).

The main advantage of ICL is that it does not require the experimental images to be intensity normalised. A systematic error or scaling can easily be incorporated or alternatively it can be used as an independent method of atom counting. The limitations of the ICL approach have also been covered by Van Aert (51) and De Backer *et al.* (60). In particular the field of view and therefore the number of observations per Gaussian component greatly affect the ability of the ICL criterion to estimate the correct number of components. This is critical for investigations of nanomaterials where their finite size severely limits the number of observations available per component, but could potentially be overcome by

combining several images for incorporation into the histogram (31).

### 3.4 Three-Dimensional Reconstruction

The traditional method for three-dimensional (3D) reconstruction is electron tomography (61), developed from X-ray tomography (62). A 3D structure is reconstructed from a tilt series of images using one of a variety of possible reconstruction algorithms (63, 64). The main requirement is for the micrographs to be ‘true projections of the structure’ (65) such that image intensities are a monotonic function of sample thickness. Therefore the use of TEM or BF-STEM is not desirable because Fresnel fringes and diffraction contrast are a significant problem. Tomography was initially developed for biological samples (66, 67) and is regularly used to determine the location of catalysts particles on their supports (68–73). Once the 3D shape has been reconstructed important information such as surface area, volume and thickness distributions can be measured for particles (74). Carrying out tomographic reconstructions by this method subjects the sample to high amounts of electron dose from the hundred images required for a single reconstruction and the dose inflicted during any tilting and re-centring processes between frames.

The more recent method of discrete tomography (75) significantly reduces the number of necessary projections to less than 10, even in the presence of noise or defects, through the use of ‘prior knowledge’. Atomic resolution discrete tomography (59) uses the prior knowledge that the particles have crystalline structure, contain no voids and surface steps and kinks are minimised. This is primarily carried out by defining each crystallographic point as a boxed region and then only one atom may lie within each box.

Van Aert *et al.* were the first group to publish atomic resolution discrete tomography data on their embedded silver nanoparticle (59) and also the core of core-shell semi-conductor nanocrystals (76). In their research they found that two or three quantified HAADF STEM images down crystallographic orientations (for example [100], [010] and [110]) gave sufficient information to reconstruct the particle, provided the atoms are restricted to a particular, in this case face-centred cubic (fcc), crystalline structure. Their quantitative STEM method (57) was used on each projection image to estimate the number of atoms before carrying out a reconstruction. It is, however, important to note that both of the example particles used to demonstrate this method had been



embedded in another material, thereby limiting the surface mobility and improving the dose tolerance for such reconstructions to be carried out.

A more recent alternative to tomography has been designed specifically for the study of free standing catalysts where the mobility of surface atoms between sequential images will be high. Using the method of quantitative STEM with scattering cross-sections, an automated procedure has been developed for peak finding (to find each atomic column location within an image) and subsequently estimating the number of atoms they contain (77). Armed with the atomic column locations and the number of atoms it becomes possible to estimate the 3D structure from only one experimental image (see Figure 7). The same assumptions described above for atomic resolution discrete tomography are combined with atomic spacing in the beam direction predicted from bulk crystal

information. A significant advantage to this approach is the requirement of only one experimental image for 3D information. This not only provides reduced dose capabilities but also increases throughput, leading to the ability to reconstruct a time series of images (77) or several particles in one sample (47, 78).

#### 4. Composition Analysis

The STEM image intensity contains both composition and thickness information which can be difficult to differentiate. A particular example of this is acid leached platinum cobalt nanoparticles; the increased ADF image intensity of the heavy metal shell is swamped by the loss in intensity due to the large reduction in sample thickness at the particle surface (79, 80). The challenge facing quantification of bimetallic systems is how to incorporate additional

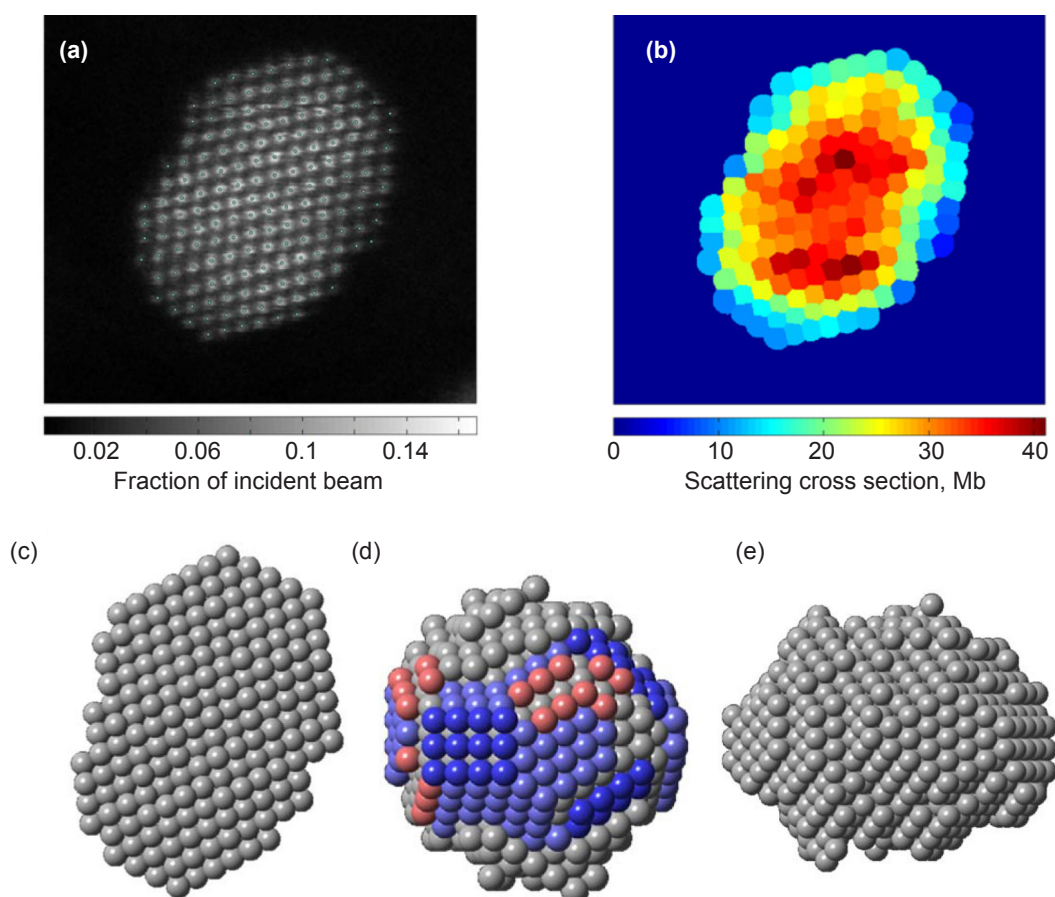


Fig. 7. Particle 3 – normalised experimental ADF image (a) of a Pt/Ir particle with the calculated cross-section map; (b) the 3D reconstructed particle is shown parallel to the beam direction; (c) perpendicular to the beam direction at from two angles  $90^\circ$  from each other (d) and (e). For ease of comparison with a Wulff construction the (d) projection has had the faces coloured in,  $\{111\}$  purple,  $\{100\}$  blue,  $\{110\}$  red



information or assumptions in order to separate out the thickness and composition contributions from the ADF STEM signal. For PEMFCs in particular it is desirable to understand how much Pt there is and its location on the particle surfaces.

A combination of sequential high resolution STEM images and multi-slice simulation has been successfully implemented by Ortalan *et al.* (81) on Ir-Rh clusters, using intensity ratios to predict possible combinations of iridium and rhodium in each column. This procedure, however, was only possible due to the small size of the clusters investigated (containing a maximum of three atoms per column); at larger particle sizes with an exponential increase in the number of possible combinations this approach quickly becomes unrealistic. Carlino and Grillo (82, 83) demonstrated that it is possible to use a section of sample with known composition to interpolate the thickness where composition is unknown to estimate composition changes on a relative scale. Rosenauer *et al.* have extended this approach at atomic resolution analysis (49, 84). However, this technique is rather limited to the semiconductor multilayer systems for which it was designed, where areas of known composition are present in the same image. Molina (85, 86) and Hernández-Maldonado *et al.* (87) have demonstrated approaches using a series of carefully controlled reference samples with accurately known composition, although this comes with its own problems of being able to manufacture such standards.

With these restrictions to quantitative ADF STEM for compositional analysis it is therefore useful to look at the other available signals which an electron microscope can provide. Elemental analysis of catalyst particles began as early as 1983 (88). The advantage of using so-called microanalysis in the electron microscope is the ability to achieve compositional information at the same length scale as the electron micrographs thereby providing invaluable local microstructural information of a sample. Here the focus is on EDX, one of the two microanalysis techniques which can be carried out within a TEM/STEM. EDX analysis relies on the excitation and ejection of an inner shell electron within an atom in the sample. An outer shell electron fills the subsequent hole whilst emitting an X-ray of characteristic energy. The EDX signal has significantly worse SNR than ADF but the elemental information is much more readily separable. The alternative technique, electron energy loss spectroscopy (EELS), provides higher count rates but in many cases can

prove challenging to use for mapping of several elements at the same time. This is especially true for heavy elements like Pt (89) where the ionisation edge is very high energy. Microanalysis is a region where STEM demonstrates advantages over TEM due to the focused probe providing localised information and the ability to collect ADF and microanalysis signals simultaneously.

Aberration correction has produced a significant advancement for microanalysis, particularly in the realms of 2D elemental mapping due to the significant increase in current density within the finer corrected probe. However for samples prone to beam damage this high current density is a problem. For mapping in particular, one must be aware of the damage being caused by the long acquisition times in order to improve total counts (90). From experience (47) it has been found that this damage can be minimised through using sequential fast scanning, where several fast acquisitions of a line scan or map are combined, to reduce the dwell time per pixel per scan while still maintaining the total live time necessary for high counts. Ideally sub-pixel scanning is also used so the beam is never stationary over the sample. It is unclear why such an approach yields lower damage unless the lower dose rate per pixel allows sufficient time for the charge or heat to dissipate away from the analysis region into the remainder of the sample.

Even without aberration correction Prestvik *et al.* carried out some of the earliest investigations into STEM-EDX analysis of bimetallic nanoparticles where individual platinum-rhenium particles sized 0.5–2.5 nm were imaged and the percentage Pt was plotted against particle size (91). EDX mapping has been used to demonstrate the localisation of sulfur on the nanoparticles in ‘poisoned’ catalysts (90). In more recent years EDX of 5 nm core-shell nanoparticles mapping has been able to differentiate the layered structure very effectively (89); however the atomic columns are not resolved due to the trade-off between resolution and counts. Deepak *et al.* (89) have demonstrated the use of multivariate statistical analysis (92) to improve their quantification, mining their data cube for independently varying compositions.

The new generation of EDX detectors has provided a huge advancement for the field of TEM microanalysis. The improved detector design of these silicon drift detectors (SDD) (93–95) allows for larger devices and therefore increased solid angles for X-ray collection. They are also often windowless which allows them

to be located closer to the sample thereby increasing the improved solid angle of collection (up to 1.3 srad, whereas previous generation detectors only reached up to 0.3 srad). The improvement in X-ray count rates is sufficient that atomic resolution maps (96–99) and X-ray tomography (100) are now both regularly possible in reasonable time scales. Tran *et al.* are among the first to apply these new detectors to nanoparticles (101), allowing them to map their copper-gold nanoparticles ranging 1–10 nm in diameter. No comment or attempt is made towards quantification of the alloy ratio apart from establishing their particles as random alloys.

## 5. Quantification of Energy Dispersive X-ray

SDD have opened up a new era in microanalysis. Combining their improved collection efficiency with the higher current densities provided by aberration correction (16, 19) yields a huge increase in X-ray counts leading to the potential for improved quantitative analysis. This is particularly relevant when investigating catalyst nanoparticles where only a small number of counts are generated from the low mass of sample.

Quantification through direct comparison with simulations (98) must take into account both X-ray absorption and subsequent re-fluorescence. This requires knowledge of, or estimation of, local thickness and density (although this can be neglected for thin specimens such as nanoparticles). The detector geometry and detection efficiency must also be included in quantification calculations, including both the solid collection angle and the take-off angle.

### 5.1 k-Factors and $\zeta$ -Factors

The original ratio approach to EDX quantification in TEM thin films was first proposed by Cliff and Lorimer nearly forty years ago (102). The Cliff-Lorimer or k-factor,  $k_{AB}$ , relates the atomic fractions,  $C_A$  and  $C_B$ , of constituent elements A and B to their measured X-ray intensities,  $I_A$  and  $I_B$  (Equation (i)).

$$\frac{C_A}{C_B} = k_{AB} \frac{I_A}{I_B} \quad (i)$$

In the technique's infancy a ratio approach was essential due to the mechanical and electrical instabilities present in the early analytical electron microscopes and therefore the low X-ray counts detected. Electron microscope capabilities are now considerably improved, especially the beam current stability. Despite this the k-factor approach remains

the primary method for EDX quantification due to its incorporation into the majority of commercial analysis software. Most EDX software allows a quantification option, however it is a rather 'black box' approach meaning it is not necessarily clear which methods of count extraction are being used.

The k-factors used in software have normally been calculated from first principle quantum mechanics. These theoretical k-factors have a minimum estimated systematic error of around 10% (103) but this could be as high as 20% (104). The only way to reduce such an error is to calculate an experimental k-factor by analysing a set of known samples with very similar density and thickness at a range of compositions to create a calibration curve ( $\sim \pm 1\%$  error is achievable). Unfortunately, this is time consuming and there is an inherent difficulty in manufacturing such samples where the composition is homogenous on the nanoscale and corresponds to the macroscopic chemical composition determined by other methods.

An alternative to the k-factor approach is the  $\zeta$  (zeta)-factor (104, 105) method first proposed in 1996 by Watanabe *et al.* (105). Designed for thin film specimens it makes use of pure element standards which are rather more readily available than the alloy alternatives, Equation (ii):

$$\rho t = \zeta_x \frac{I_x}{C_x D_e} \quad (ii)$$

$\zeta_x$  is the factor connecting  $I_x$ , the raw X-ray counts, to  $\rho t$ , the total density multiplied by sample thickness.  $C_x$  is the weight fraction of x, with a similar relationship holding independently for other elements in the system. It assumes that the characteristic X-ray intensity from element A,  $I_A$ , is proportional to the mass-thickness of the sample. This holds well as long as X-ray absorption and fluorescence are negligible, which is the case for thin specimens; for thicker specimens an absorption correction should also be incorporated (106), (Equation (iii))

$$D_e = N_e i_p \tau \quad (iii)$$

$D_e$  is the total number of electrons seen by the sample during acquisitions defined in terms of  $N_e$ , the number of electrons in a unit electric charge (or  $1/e$ ), the probe current,  $i_p$ , and the acquisition time,  $\tau$ . The  $\zeta$ -factor, therefore, is independent of acquisition time, beam current, composition and mass-thickness providing it with units of kg electron  $m^{-2}$  photon $^{-1}$ .

It is vital to know the beam current at the time of analysis by a direct measurement (for example, Faraday cup) in order to calculate the dose. Whilst this method may seem less trivial as it requires thickness calibration and current measurements it does have the significant advantage that pure element thin films can be used as standards (107), which are often more routinely available. This method can prove more accurate than the k-factor method and is an absolute value rather than a ratio based on other elements within the system. It can also be used as a method of instrumentation comparison, to evaluate which microscopes have better analytical capabilities.

## 5.2 Accuracy Limitations

The key problem with STEM EDX of nanoparticles (108–110) is the limited count rate because of the small number of atoms excited. For example, in early maps produced by Lyman (88) in 1987 the number of counts from a background area pixel was 7 whilst the maximum number of counts from a Pd pixel was only 36 (giving a  $\sqrt{N}$  error of 18.5%). The problem with EDX is finding the balance between high beam currents for improved analytical resolution which increases the probe diameter or keeping the probe diameter small for improved spatial resolution but which results in poor counting statistics. E *et al.* (42) confirmed that the limiting factor for EDX of nanoparticles will be in achieving high enough counts of characteristic X-rays where beam sensitive samples place restrictions on the length of acquisition possible. A low number of counts results in poor statistics, reducing the reliability of quantification. There is a thickness dependent error in quantification (80) because a thicker region of sample will produce more raw X-ray counts and so have a smaller statistics error.

Another fundamental limitation for accurate STEM EDX quantification is absorption of X-ray photons before they are able to escape the sample, although this becomes less of a problem for thinner samples like nanomaterials. The absorption rate is element specific, so could cause an error in the quantification results. Work by Watanabe and Williams (104) has demonstrated the effects of both the sample thickness and X-ray line selection on EDX quantification. For the very small sample thicknesses of nanoparticles any K or L lines will provide sufficient quantification accuracy; however the M-lines may still provide small absorption errors and should therefore be avoided where possible. For elements with an atomic number lower than 30,

quantification should only be carried out with the K-lines as the L-lines also begin to drop below the safe limit. Often the degree of absorption occurring within the sample can be estimated through the K-line to L-line height ratios because the L-lines begin to be absorbed much sooner, thereby changing the peak height ratios.

## 5.3 Energy Dispersive X-ray Cross-sections

The most recent method for quantification is by calculating cross-sections. EDX partial cross-sections (79) provide a robust measure which is easy to compare with the scattering cross-sections used for ADF STEM quantification (23, 29, 77) and ionisation edges in EELS (111–113). In sufficiently thin samples, not aligned along a low order zone-axis, so that channelling, X-ray absorption and fluorescence can be neglected, the number of X-ray counts is linearly proportional to sample thickness. The EDX partial cross-section of a single atom can therefore be determined from a polycrystalline pure element wedge sample with known wedge angle using Equation (iv) (79):

$$\sigma_x = \frac{e}{i\tau n_x \tan(\theta)} \cdot \frac{dl_x}{dx} \quad (\text{iv})$$

where  $e$  is unit electronic charge,  $i$  is the probe current,  $\tau$  is the total pixel dwell time,  $n_x$  is the atomic density of the element  $x$  and  $\theta$  is the wedge angle.  $dl_x/dx$  is the gradient extracted from a line profile showing integrated X-ray counts plotted against distance into the sample. Further details about this calibration method and its accuracy can be found in the literature (79).

Cross-sections are specific to a given microscope setup, including the solid-angle and collection efficiency of the EDX detector, as well as the microscope operating voltage, making them a good comparison tool between analytical TEMs. Such calibrations are also dependent on the specific X-ray peaks used, as well as the chosen energy window and background subtraction method, but this is also true for  $k$  and  $\zeta$ -factors. The cross-section approach can provide atomic counts on an absolute scale which negates the need for knowledge of sample thickness, particularly useful for nanoparticles where the exact thickness can be difficult to determine.

EDX cross-section quantification has been applied to acid leached PtCo nanoparticles in order to determine the depth of the Pt enrichment produced by the leaching process (79, 80). With Pt(Pd) core-shell nanoparticles it is possible to characterise the non-uniformity of the Pt shell (see [Figure 8](#)). The intended two-monolayer

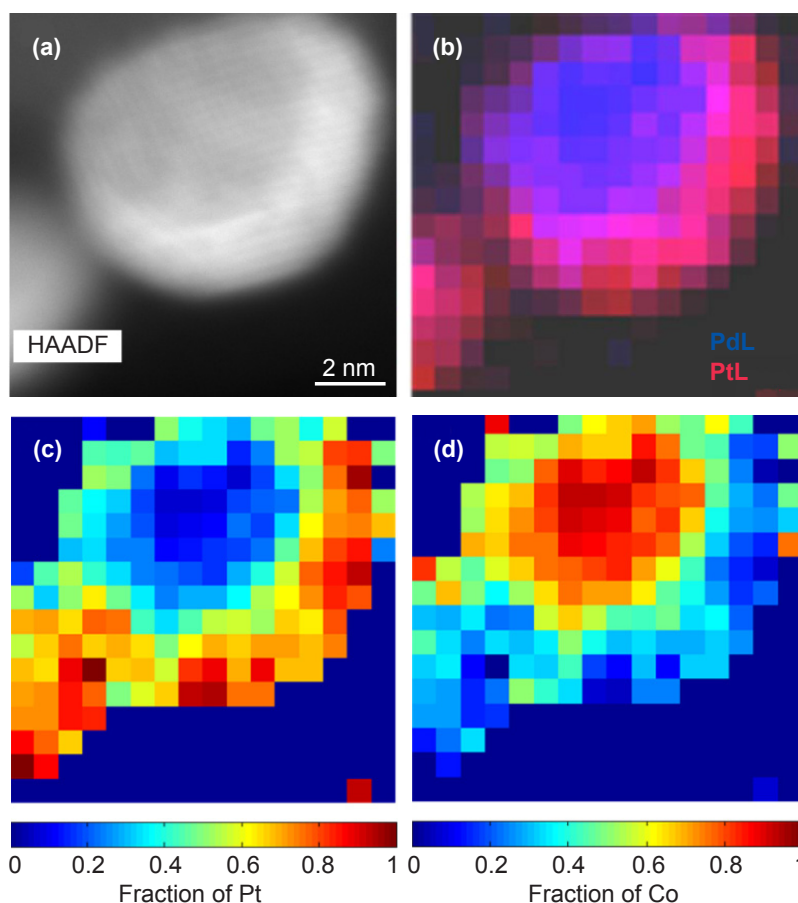


Fig. 8. A 6–7 nm particle demonstrating the more usual Pt capping of the particles, with overall composition of 45.4% Pt. (a) The cumulative STEM image shows a clear step contrast variation towards the particle surface; (b) the composite image; (c) the fractional Pt and (d) Pd maps show distinct Pd core with a Pt rich cap covering two thirds of the particle edge. The Pt shell cannot cover where the particle is sitting on the carbon black support

coverage actually results in a thicker than two-monolayer coverage over part of the particle surface. The Pt shell is applied after the particles have been deposited onto the carbon support which limits the amount of coverage which can occur due to the position of the particles' contact with the particle support.

## 6. Conclusions

The new developments in STEM characterisation now make it possible to pursue sub-particle and even atomic resolution compositional and structural information about nanomaterials in a genuinely quantitative manner. Whilst this approach should still be combined with more broad-beam techniques, such as X-ray or infrared spectroscopy, with much better statistical representation, the movement towards automation is beginning to allow for several particles to be analysed. Such atomic-scale

information is invaluable in the work towards catalyst understanding and design. The beam sensitive nature of catalyst nanoparticles puts restrictions on the acquisition time for microanalysis. However in STEM multiple signals can be collected in parallel. Therefore creating a cross-section method for quantification which is comparable across multiple signals opens the way for combining the information they provide to yield more fruitful results.

## 7. Acknowledgments

K. MacArthur gratefully acknowledges the financial support of the Engineering and Physical Sciences Research Council (EPSRC) and Johnson Matthey towards her DPhil. She is also indebted to the support of both research groups at the University of Oxford and her supervisors Dogan Ozkaya, Peter Nellist and Sergio Lozano-Perez.



## References

- 1 A. V. Crewe, J. Wall and J. Langmore, *Science*, 1970, **168**, (3937), 1338
- 2 P. D. Nellist and S. J. Pennycook, *Science*, 1996, **274**, (5286), 413
- 3 J. I. Goldstein, D. E. Newbury, P. Echlin, D. C. Joy, C. E. Lyman, E. Lifshin, L. Sawyer and J. R. Michael, "Scanning Electron Microscopy and X-ray Microanalysis", 3rd Edn., Springer Science+Business Media, New York, USA, 2003
- 4 D. B. Williams and C. B. Carter, "Transmission Electron Microscopy: A Textbook for Materials Science", 2nd Edn., Springer Science+Business Media, New York, USA, 2009
- 5 A. P. Pogany and P. S. Turner, *Acta Cryst. A*, 1968, **24**, 103
- 6 S. Lee, Y. Oshima, H. Sawada, F. Hosokawa, E. Okunishi, T. Kaneyama, Y. Kondo, S. Niitaka, H. Takagi, Y. Tanishiro and K. Takayanagi, *J. Appl. Phys.*, 2011, **109**, (11), 113530
- 7 S. D. Findlay, S. Azuma, N. Shibata, E. Okunishi and Y. Ikuhara, *Ultramicroscopy*, 2011, **111**, (4), 285
- 8 E. Okunishi, H. Sawada and Y. Kondo, *Micron*, 2012, **43**, (4), 538
- 9 A. Howie, *J. Microsc.*, 1979, **117**, (1), 11
- 10 A. Amali and P. Rez, *Microsc. Microanal.*, 1997, **3**, (1), 28
- 11 Z. W. Wang, Z. Y. Li, S. J. Park, A. Abdela, D. Tang and R. E. Palmer, *Phys. Rev. B*, 2011, **84**, (7), 073408
- 12 T. F. Budinger and R. M. Glaeser, *Ultramicroscopy*, 1976–1977, **2**, 31
- 13 O. Scherzer, *Z. Phys.*, 1936, **101**, (9), 593
- 14 F. Haguénau, P. W. Hawkes, J. L. Hutchison, B. Satiat-Jeunemaître, G. T. Simon and D. B. Williams, *Microsc. Microanal.*, 2003, **9**, (2), 96
- 15 P. Xu, E. J. Kirkland, J. Silcox and R. Keyse, *Ultramicroscopy*, 1990, **32**, (2), 93
- 16 O. L. Krivanek, N. Dellby, A. J. Spence, R. A. Camps and L. M. Brown, *Electron Microsc. Anal.*, 1997, **153**, 35
- 17 P. D. Nellist, M. F. Chisholm, N. Dellby, O. L. Krivanek, M. F. Murfitt, Z. S. Szilagy, A. R. Lupini, A. Borisevich, W. H. Sides Jr. and S. J. Pennycook, *Science*, 2004, **305**, (5691), 1741
- 18 H. Müller, S. Uhlemann, P. Hartel and M. Haider, *Microsc. Microanal.*, 2006, **12**, (6), 442
- 19 P. E. Batson, N. Dellby and O. L. Krivanek, *Nature*, 2002, **418**, (6898), 617
- 20 S. C. Anderson, C. R. Birkeland, G. R. Anstis and D. J. H. Cockayne, *Ultramicroscopy*, 1997, **69**, (2), 83
- 21 R. Darji and A. Howie, *Micron*, 1997, **28**, (2), 95
- 22 M. J. Hytch and W. M. Stobbs, *Ultramicroscopy*, 1994, **53**, (3), 191
- 23 M. Retsky, *Optik*, 1974, **41**, 127
- 24 M. S. Isaacson, D. Kopf, M. Ohtsuki and M. Utlaut, *Ultramicroscopy*, 1979, **4**, (1), 101
- 25 N. P. Young, Z. Y. Li, Y. Chen, S. Palomba, M. Di Vece and R. E. Palmer, *Phys. Rev. Lett.*, 2008, **101**, (24), 246103
- 26 A. Singhal, J. C. Yang and J. M. Gibson, *Ultramicroscopy*, 1997, **67**, (1–4), 191
- 27 S. E. Maccagnano-Zacher, K. A. Mkhoyan, E. J. Kirkland and J. Silcox, *Ultramicroscopy*, 2008, **108**, (8), 718
- 28 D. Van Dyck and M. Op de Beeck, *Ultramicroscopy*, 1996, **64**, (1–4), 99
- 29 H. E. K. E. MacArthur, T. J. Pennycook, E. Okunishi, A. J. D'Alfonso, N. R. Lugg, L. J. Allen and P. D. Nellist, *Ultramicroscopy*, 2013, **133**, 109
- 30 E. Rotunno, M. Albrecht, T. Markurt, T. Remmele and V. Grillo, *Ultramicroscopy*, 2014, **146**, 62
- 31 A. De Backer, G. T. Martinez, K. E. MacArthur, L. Jones, A. Béché, P. D. Nellist and S. Van Aert, *Ultramicroscopy*, 2015, **151**, 56
- 32 K. E. MacArthur, A. J. D'Alfonso, D. Ozkaya, L. J. Allen and P. D. Nellist, *Ultramicroscopy*, 2015, **156**, 1
- 33 R. F. Loane, E. J. Kirkland and J. Silcox, *Acta Cryst. A*, 1988, **44**, 912
- 34 J. Hwang, J. Y. Zhang, A. J. D'Alfonso, L. J. Allen and S. Stemmer, *Phys. Rev. Lett.*, 2013, **111**, (26–27), 266101
- 35 P. M. Voyles, D. A. Muller and E. J. Kirkland, *Microsc. Microanal.*, 2004, **10**, (2), 291
- 36 P. M. Voyles, J. L. Grazul and D. A. Muller, *Ultramicroscopy*, 2003, **96**, (3–4), 251
- 37 R. Ishikawa, A. R. Lupini, S. D. Findlay, T. Taniguchi and S. J. Pennycook, *Nano Lett.*, 2014, **14**, (4), 1903
- 38 J. M. LeBeau and S. Stemmer, *Ultramicroscopy*, 2008, **108**, (12), 1653
- 39 A. Rosenauer, K. Gries, K. Müller, A. Pretorius, M. Schowalter, A. Avramescu, K. Engl and S. Lutgen, *Ultramicroscopy*, 2009, **109**, (9), 1171
- 40 Z. Yu, P. E. Batson and J. Silcox, *Ultramicroscopy*, 2003, **96**, (3–4), 275
- 41 H. E. 'Quantitative Analysis of Core-Shell Nanoparticle Catalysts by Scanning Transmission Electron

- Microscopy', DPhil Thesis, University of Oxford, UK, 2013
- 42 H. E. P. D. Nellist, S. Lozano-Perez and D. Ozkaya, *J. Phys.: Conf. Ser.*, 2010, **241**, (1), 012067
- 43 S. D. Findlay and J. M. LeBeau, *Ultramicroscopy*, 2013, **124**, 52
- 44 K. E. MacArthur, L. B. Jones and P. D. Nellist, *J. Phys.: Conf. Ser.*, 2014, **522**, 012018
- 45 G. T. Martinez, L. Jones, A. De Backer, A. Béch , J. Verbeeck, S. Van Aert and P. D. Nellist, *Ultramicroscopy*, 2015, **159**, (1), 46
- 46 J. M. LeBeau, S. D. Findlay, L. J. Allen and S. Stemmer, *Nano Lett.*, 2010, **10**, (11), 4405
- 47 K. E. MacArthur, 'Quantitative Structural and Compositional Characterisation of Bimetallic Fuel-Cell Catalyst Nanoparticles Using STEM', DPhil Thesis, University of Oxford, UK, 2015
- 48 G. T. Martinez, A. De Backer, A. Rosenauer, J. Verbeeck and S. Van Aert, *Micron*, 2014, **63**, 57
- 49 A. Rosenauer, T. Mehrtens, K. M ller, K. Gries, M. Schowalter, P. V. Satyam, S. Bley, C. Tessarek, D. Hommel, K. Sebald, M. Seyfried, J. Gutowski, A. Avramescu, K. Engl and S. Lutgen, *Ultramicroscopy*, 2011, **111**, (8), 1316
- 50 D. T. Nguyen, S. D. Findlay and J. Etheridge, *Ultramicroscopy*, 2014, **146**, 6
- 51 S. Van Aert, A. De Backer, G. T. Martinez, B. Goris, S. Bals, G. Van Tendeloo and A. Rosenauer, *Phys. Rev. B*, 2013, **87**, (6), 064107
- 52 V. Grillo and F. Rossi, *Ultramicroscopy*, 2013, **125**, 112
- 53 A. Re nik, G. M bus and S.   Sturm, *Ultramicroscopy*, 2005, **103**, (4), 285
- 54 A. B. Yankovich, B. Berkels, W. Dahmen, P. Binev, S. I. Sanchez, S. A. Bradley, A. Li, I. Szlufarska and P. M. Voyles, *Nature Commun.*, 2014, **5**, 4155
- 55 L. Jones, H. Yang, T. J. Pennycook, M. S. J. Marshall, S. Van Aert, N. D. Browning, M. R. Castell and P. D. Nellist, *Adv. Struct. Chem. Imaging.*, 2015, **1**, 8
- 56 A. J. den Dekker, S. Van Aert, A. van den Bos and D. Van Dyck, *Ultramicroscopy*, 2005, **104**, (2), 83
- 57 S. Van Aert, J. Verbeeck, R. Erni, S. Bals, M. Luysberg, D. Van Dyck and G. Van Tendeloo, *Ultramicroscopy*, 2009, **109**, (10), 1236
- 58 R. Erni, H. Heinrich and G. Kosterz, *Ultramicroscopy*, 2003, **94**, (2), 125
- 59 S. Van Aert, K. J. Batenburg, M. D. Rossell, R. Erni and G. Van Tendeloo, *Nature*, 2011, **470**, (7334), 374
- 60 A. De Backer, G. T. Martinez, A. Rosenauer and S. Van Aert, *Ultramicroscopy*, 2013, **134**, 23
- 61 D. J. De Rosier and A. Klug, *Nature*, 1968, **217**, (5124), 130
- 62 B. P. Flannery, H. W. Deckman, W. G. Roberge and K. L. D'Amico, *Science*, 1987, **237**, (4821), 1439
- 63 N. Kawase, M. Kato, H. Nishioka and H. Jinnai, *Ultramicroscopy*, 2007, **107**, (1), 8
- 64 C. K bel, D. Niemeyer, R. Cieslinski and S. Rozeveld, *Mater. Sci. Forum*, 2010, **638–642**, 2517
- 65 M. Weyland, *Top. Catal.*, 2002, **21**, (4), 175
- 66 D. E. Jesson and S. J. Pennycook, *Proc. Roy. Soc. Lond.*, 1995, **449**, (1936), 273
- 67 K. K. Nanda, A. Maisels, F. E. Kruis, H. Fissan and S. Stappert, *Phys. Rev. Lett.*, 2003, **91**, (10), 106102
- 68 A. J. Koster, U. Ziese, A. J. Verkleij, A. H. Janssen and K. P. de Jong, *J. Phys. Chem. B.*, 2000, **104**, (40), 9368
- 69 J. R. Jinschek, K. J. Batenburg, H. A. Calderon, R. Kilaas, V. Radmilovic and C. Kisielowski, *Ultramicroscopy*, 2008, **108**, (6), 589
- 70 L. C. Gontard, R. E. Dunin-Borkowski, D. Ozkaya, T. Hyde, P. A. Midgley and P. Ash, *J. Phys.: Conf. Ser.*, 2006, **26**, 367
- 71 G. M bus and B. J. Inkson, *Appl. Phys. Lett.*, 2001, **79**, (9), 1369
- 72 R. Grothausmann, S. Fiechter, R. Beare, G. Lehmann, H. Kropf, G. S. V. Kumar, I. Manke and J. Banhart, *Ultramicroscopy*, 2012, **122**, 65
- 73 H. Friedrich, S. Guo, P. E. de Jongh, X. Pan, X. Bao and K. P. de Jong, *ChemSusChem*, 2011, **4**, (7), 957
- 74 S. Sueda, K. Yoshida and N. Tanaka, *Ultramicroscopy*, 2010, **110**, (9), 1120
- 75 K. J. Batenburg and J. Sijbers, *IEEE Trans. Image Process.*, 2011, **20**, (9), 2542
- 76 S. Bals, M. Casavola, M. A. van Huis, S. Van Aert, K. J. Batenburg, G. Van Tendeloo and D. Vanmaekelbergh, *Nano Lett.*, 2011, **11**, (8), 3420
- 77 L. Jones, K. E. MacArthur, V. T. Fauske, A. T. J. van Helvoort and P. D. Nellist, *Nano Lett.*, 2014, **14**, (11), 6336
- 78 K. E. MacArthur, L. B. Jones, S. Lozano-Perez, D. Ozkaya and P. D. Nellist, 'Quantification of Pt/Ir Catalyst Nanoparticles using ADF STEM' in 18th International Microscopy Congress, Prague, Czech Republic, 7–12th September, 2014
- 79 K. E. MacArthur, T. J. A. Slater, S. J. Haigh, D. Ozkaya, P. D. Nellist and S. Lozano-Perez, *Microsc. Microanal.*, 2016, **22**, (1), 71
- 80 K. E. MacArthur, T. J. A. Slater, S. J. Haigh, D. Ozkaya, P. D. Nellist and S. Lozano-Perez, *Mater. Sci. Technol.*, 2016, doi:10.1080/02670836.2015.1133021

- 81 V. Ortalan, A. Uzun, B. C. Gates and N. D. Browning, *Nature Nanotechnol.*, 2010, **5**, (12), 843
- 82 E. Carlino and V. Grillo, *Phys. Rev. B.*, 2005, **71**, (23), 235303
- 83 V. Grillo, *Ultramicroscopy*, 2009, **109**, (12), 1453
- 84 A. Rosenauer, K. Gries, K. Müller, M. Schowalter, A. Pretorius, A. Avramescu, K. Engl and S. Lutgen, *J. Phys.: Conf. Ser.*, 2010, **209**, (1), 012009
- 85 S. I. Molina, D. L. Sales, P. L. Galindo, D. Fuster, Y. González, B. Alén, L. González, M. Varela and S. J. Pennycook, *Ultramicroscopy*, 2009, **109**, (2), 172
- 86 S. I. Molina, M. P. Guerrero, P. L. Galindo, D. L. Sales, M. Varela and S. J. Pennycook, *J. Electron Microsc. (Tokyo)*, 2011, **60**, (1), 29
- 87 D. Hernández-Maldonado, M. Herrera, P. Alonso-González, Y. González, L. González, J. Gazquez, M. Varela, S. J. Pennycook, M. de la Paz Guerrero-Lebrero, J. Pizarro, P. L. Galindo and S. I. Molina, *Microsc. Microanal.*, 2011, **17**, (4), 578
- 88 C. E. Lyman, *J. Mol. Catal.*, 1983, **20**, (3), 357
- 89 F. L. Deepak, G. Casillas-Garcia, R. Esparza, H. Barron and M. Jose-Yacamán, *J. Cryst. Growth*, 2011, **325**, (1), 60
- 90 J. J. Friel and C. E. Lyman, *Microsc. Microanal.*, 2006, **12**, (1), 2
- 91 R. Prestvik, B. Tøtdal, C. E. Lyman and A. Holmen, *J. Catal.*, 1998, **176**, (1), 246
- 92 J. M. Titchmarsh, *Micron*, 1999, **30**, (2), 159
- 93 P. Lechner, C. Fiorini, R. Hartmann, J. Kemmer, N. Krause, P. Leutenegger, A. Longoni, H. Soltau, D. Stötter, R. Stötter, L. Strüder and U. Weber, *Nucl. Instr. Methods Phys. Res. A.*, 2001, **458**, (1–2), 281
- 94 H. S. von Harrach, P. Dona, B. Freitag, H. Soltau, A. Niculae and M. Rohde, *J. Phys.: Conf. Ser.*, 2010, **241**, (1), 012015
- 95 P. J. Phillips, T. Paulauskas, N. Rowlands, A. W. Nicholls, K.-B. Low, S. Bhadare and R. F. Klie, *Microsc. Microanal.*, 2014, **20**, (4), 1046
- 96 L. J. Allen, A. J. D'Alfonso, B. Freitag and D. O. Klenov, *MRS Bull.*, 2012, **37**, (1), 47
- 97 M. Itakura, N. Watanabe, M. Nishida, T. Daio and S. Matsumura, *Jpn. J. Appl. Phys.*, **52**, (5R), 050201
- 98 G. Kothleitner, M. J. Neish, N. R. Lugg, S. D. Findlay, W. Grogger, F. Hofer and L. J. Allen, *Phys. Rev. Lett.*, 2014, **112**, (8), 085501
- 99 P. G. Kotula, D. O. Klenov and H. S. von Harrach, *Microsc. Microanal.*, 2012, **18**, (4), 691
- 100 T. J. A. Slater, P. H. C. Camargo, M. G. Burke, N. J. Zaluzec and S. J. Haigh, *J. Phys.: Conf. Ser.*, 2014, **522**, 012025
- 101 D. T. Tran, I. P. Jones, J. A. Preece, R. L. Johnston and C. R. van den Brom, *J. Nanoparticle Res.*, 2011, **13**, (9), 4229
- 102 G. Cliff and G. W. Lorimer, *J. Microsc.*, 1975, **103**, (2), 203
- 103 M. Watanabe, D. B. Williams and Y. Tomokiyo, *Micron*, 2003, **34**, (3–5), 173
- 104 M. Watanabe and D. B. Williams, *J. Microsc.*, 2006, **221**, (2), 89
- 105 M. Watanabe, Z. Horita and M. Nemoto, *Ultramicroscopy*, 1996, **65**, (3–4), 187
- 106 M. Watanabe, D. W. Ackland, C. J. Kiely, D. B. Williams, M. Kanno, R. Hynes and H. Sawada, *JEOL News*, 2006, **41**, (1), 2
- 107 D. B. Williams, A. J. Papworth and M. Watanabe, *J. Electron Microsc.*, 2002, **51**, S113
- 108 C. E. Lyman, H. G. Stenger Jr. and J. R. Michael, *Ultramicroscopy*, 1987, **22**, (1–4), 129
- 109 A. A. Herzing, M. Watanabe, J. K. Edwards, M. Conte, Z.-R. Tang, G. J. Hutchings and C. J. Kiely, *Faraday Discuss.*, 2008, **138**, 337
- 110 J. Liu, *J. Electron Microsc.*, 2005, **54**, (3), 251
- 111 W. M. Skiff, R. W. Carpenter, S. H. Lin and A. Higgs, *Ultramicroscopy*, 1988, **25**, (1), 47
- 112 F. Hofer, *Microsc. Microanal. Microstruct.*, 1991, **2**, (2–3), 215
- 113 R. F. Egerton and M. Malac, *J. Electron Spectrosc. Relat. Phenomena*, 2005, **143**, (2–3), 43

## The Author



Katherine MacArthur is currently a Helmholtz Postdoctoral Fellow at the Ernst Ruska Centre, Forschungszentrum Jülich, Germany. Her Doctorate was sponsored by Johnson Matthey at the University of Oxford, UK, which she completed in 2015. Dr MacArthur continues to look at developing techniques for improved high-resolution characterisation of catalyst nanoparticles.